NASA CR-134867

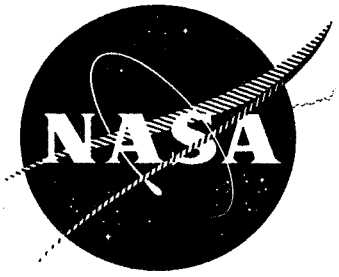

Quiet Clean Short-Haul Experimental Engine (QCSEE) Test Results from a 14 cm Inlet for a Variable Pitch Fan Thrust Reverser

by

W.F. Vier

GENERAL ELECTRIC COMPANY

Prepared For

National Aeronautics and Space Administration

NASA-Lewis Research Center
NAS3-18021

1. Report No.	2. Government Accession No.	3. Recipient's Catalog No.
NASA CR-134867		

4. Title and Subtitle	5. Report Date
QUIET, CLEAN SHORT-HAUL EXPERIMENTAL ENGINE (QCSEE) TEST RESULTS FROM A 14 cm INLET FOR VARIABLE PITCH FAN THRUST REVERSER	December 1975
	6. Performing Organization Code

7. Author(s)	8. Performing Organization Report No.
W. F. Vier Advanced Engineering & Technology Programs Department	R75AEG387
	10. Work Unit No.

9. Performing Organization Name and Address	11. Contract or Grant No.
General Electric Company Aircraft Engine Group Cincinnati, Ohio 45215	NAS3-18021
	13. Type of Report and Period Covered
12. Sponsoring Agency Name and Address	Contractor Report
National Aeronautics and Space Administration Washington, D.C. 20546	14. Sponsoring Agency Code

15. Supplementary Notes

Test Report, Project Manager: C. C. Ciepluch, QCSEE Project Office
Technical Advisor: H. L. Wesoky
NASA Lewis Research Center, Cleveland, Ohio

16. Abstract

A 1/13th scale model of the QCSEE Fan Discharge Duct was tested with a matrix of flare exlets. Exlets are flared fan nozzles configured for improved reverse-flow inlet performance for reverse-pitch fan applications. Results showed that a flare type exlet is an acceptable design for QCSEE, as indicated by high pressure recovery and low distortion performance.

17. Key Words (Suggested by Author(s))		18. Distribution Statement
Exlet	QCSEE	Unlimited
Reverse-Flow Nozzle	Inlet Recovery	
Reverse-Pitch Nozzle	Distortion	
Inlet Design	Wind Tunnel Tests	
Recovery Distortion		

19. Security Classif. (of this report)	20. Security Classif. (of this page)	21. No. of Pages	22. Price*
Unclassified	Unclassified	34	

TABLE OF CONTENTS

LIST OF ILLUSTRATIONS

LIST OF ILLUSTRATIONS (Concluded)

1.0 SUMMARY

Thirteen flared variable pitch fan thrust reverser inlet configurations were evaluated in a 1/13th scale simulation of QCSEE under-the-wing (UTW) nacelle in reverse-pitch operation. These included ten flap length/flare angle combinations, two vee-notch configurations, and one unflared flap configuration representing the forward thrust takeoff condition.

All the flare configurations provided a substantial performance benefit over the unflared (reference) configuration through:

- increased recovery [from an increase of 0.035 at 20 km/hr (10.8 kts) to 0.05 at 150 km/hr (81 kts)].
- reduced distortion (from a decrease of 0.025 at 20 km/hr to 0.06 at 150 km/hr.
- reduced tip pressure fluctuations (from ≈3% to 2%).

Improvement was demonstrated throughout the equivalent full-scale airflow range, 180 to 360 kg/sec (400 to 800 lb/sec), for nominal landing speeds of 0, 80, 115, 160 and 240 km/hr (0, 43, 62, 84 and 130 knots). All of the flared configurations performed equivalently; total pressure recoveries did not vary more than 0.01 (data bandwidth) over the tested landing speed range.

Vee notches, simulating the four nozzle leaf-to-leaf gaps, were evaluated on the scaled 45.7 cm (18 in.) flap at a 30° flare angle configuration. These few small-extent voids in the flare degraded recovery performance by less than 0.01. Small-extent, lower-pressure regions in the tip increased the circumferential distortion index by an almost negligible amount (<0.01) below 250 kg/sec full scale, and by up to 0.025 at the maximum flow rate of 360 kg/sec full scale. Local turbulence was increased, as evidenced from a 20% increase in dynamic total pressure fluctuations.

The above results indicate the flared variable pitch fan thrust reverser inlet is an acceptable design concept for the QCSEE UTW propulsion system.

2.0 INTRODUCTION

QCSEE (Quiet, Clean Short-Haul Experimental Engine) under-the-wing (UTW) design employs a reverse-pitch fan for thrust reversal upon landing. This reverse fan-flow condition requires the nozzle to function as an inlet; a nozzle that is designed for reverse flow is called an exlet. The word, exlet, consists of EX from exit and LET from inlet. The basic purpose of an exlet is to provide increased pressure recovery performance over a normal forward mode nozzle configuration in reverse flow, which is essentially equivalent to a sharp-lip, supersonic inlet at low speeds (Reference 1).

Several aerodynamic devices are applicable to nozzles for attainment of higher reversed-flow performance. This test program was an evaluation of only one type, the flare, which was chosen for the QCSEE UTW nacelle application. It was decided that the flare nozzle combined acoustic, aerodynamic and mechanical performance advantages over other devices such as slots or scoops. The QCSEE UTW flare concept is illustrated in Figure 1.

Flap length and flare angle determine the flare exlet's entrance area and thus an aerodynamic internal area-contraction ratio. A 45.7 cm (18 in.) flap length at a 30° flare angle was selected for QCSEE, on the basis that it provided a good compromise between mechanical loads (flap internal pressure at cruise and flap external pressures during landing deployment) and performance (flap boattail drag at cruise and exlet recovery performance at landing).

An isolated, powered nacelle was tested to simulate QCSEE reverse flow conditions as part of NASA's investigation of basic flare exlet configuration performance characteristics. Testing was conducted at NASA-Lewis with a General Electric model representing the current QCSEE UTW fan discharge duct and nozzle/exlet assembly. A matrix of thirteen exlet configurations was evaluated over the expected range of QCSEE reverse pitch airflows and landing speeds in order to make a selection of the most optimum flare configuration. This report summarizes the aerodynamic performance results in terms of exlet recovery and distortion.

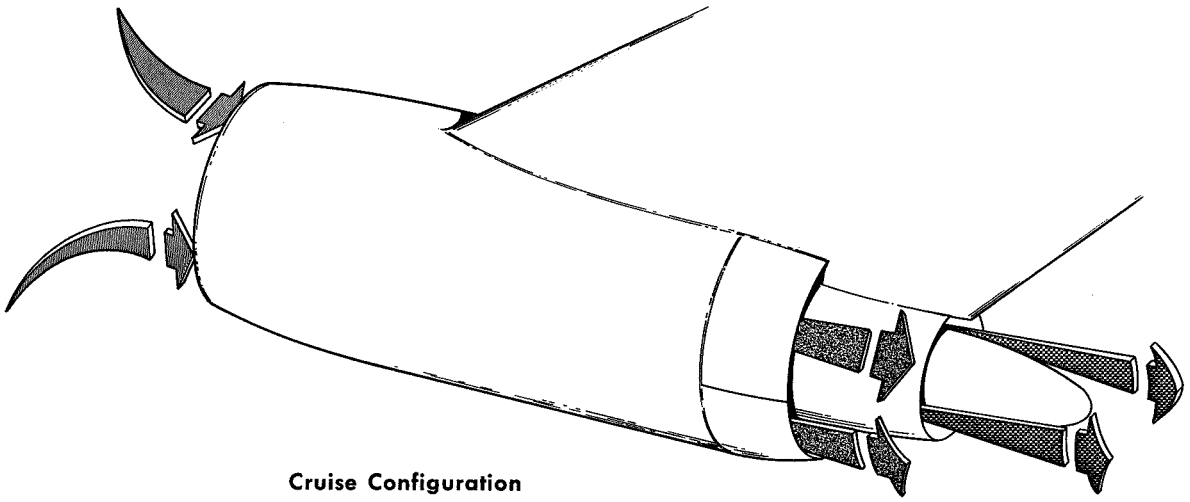

Cruise Configuration

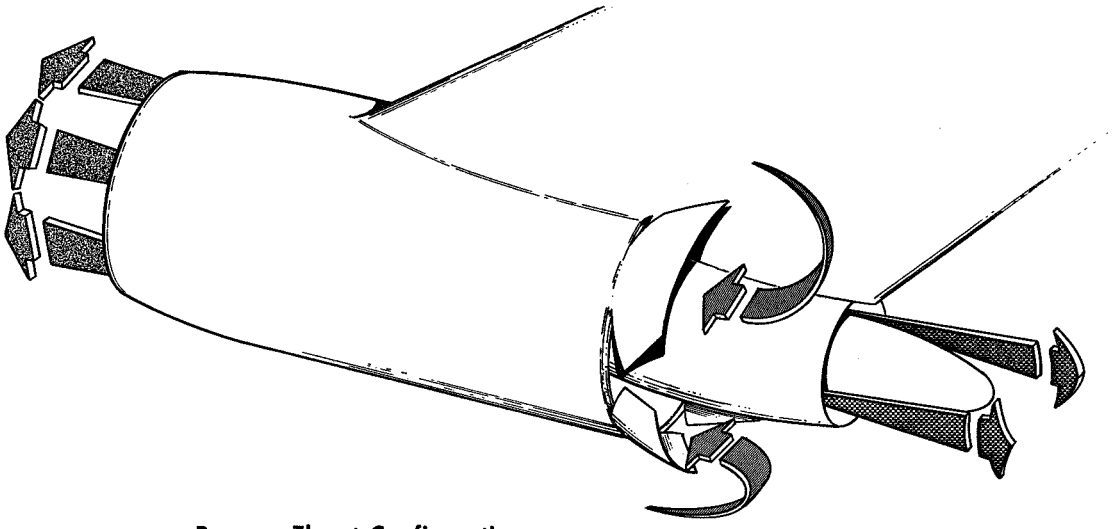

Reverse-Thrust Configuration

Figure 1. QCSEE Flare Exlet Concept.

3.0 TEST DESCRIPTION

3.1 MODEL AND SETUP

A 1/13th scale model was designed and built to represent the QCSEE UTW fan duct and nozzle/exlet assembly. Figure 2 describes the basic model and its detachable flares, while Figure 3 shows the complete nacelle, including the NASA hardware, as installed in the NASA-Lewis 9- by 15-Foot V/STOL Wind Tunnel. The model's internal contours were matched to QCSEE as seen in the comparison of model and full-scale calculated one-dimensional Mach No. distributions of Figure 4. Small differences between these Mach No. distributions were due to the lack of a pylon in the model. An attempt was made to simulate the pylon blockage via the acoustic splitter support struts. Other minor differences between this model and the engine are as follows:

- No Outlet Guide Vanes (OGV) at the measurement plane of the model (see Figure 2), as the 14 cm (5.5 in.) fan is not a reverse-pitch model.
- Not-to-scale maximum nacelle diameter due to model mechanical support, fan envelope, external instrumentation leadout.
- Mismatch of radius ratio between model fan and exlet model required a transition section (Figure 2).
- No core engine flow representation in model.

While the above are small differences, the lack of exact duplication of the deployed exlet nozzle gaps (leaf-to-leaf) at a larger scale for better Reynolds No. and mixing length simulation could have some differences in the final values; however, this is a secondary effect relative to the matching of the tunnel and fan duct Mach numbers which was accomplished through the variation of primary test conditions.

Primary model instrumentation, Plane 15 (Figure 2), was located at the simulated QCSEE outlet guide vane discharge plane, engine station = 508 cm (200 in.). Plane 15 was used for the measurement of recovery, distortion, airflow, and total pressure fluctuations (Figure 5). A series of axially aligned static pressure (P_s) taps on the basic model's cowl and plug plus four internal and four external P_s taps on three of the detachable flares were provided for mechanical load determinations.

3.2 MATRIX TESTED

A basic matrix of ten combinations of nozzle flap length and flare angle, as shown in Figure 6, was selected to span the reasonable mechanical and aerodynamic design limits for the QCSEE UTW nozzle. Two other configurations were included: A 0° flare angle representing the takeoff flap position

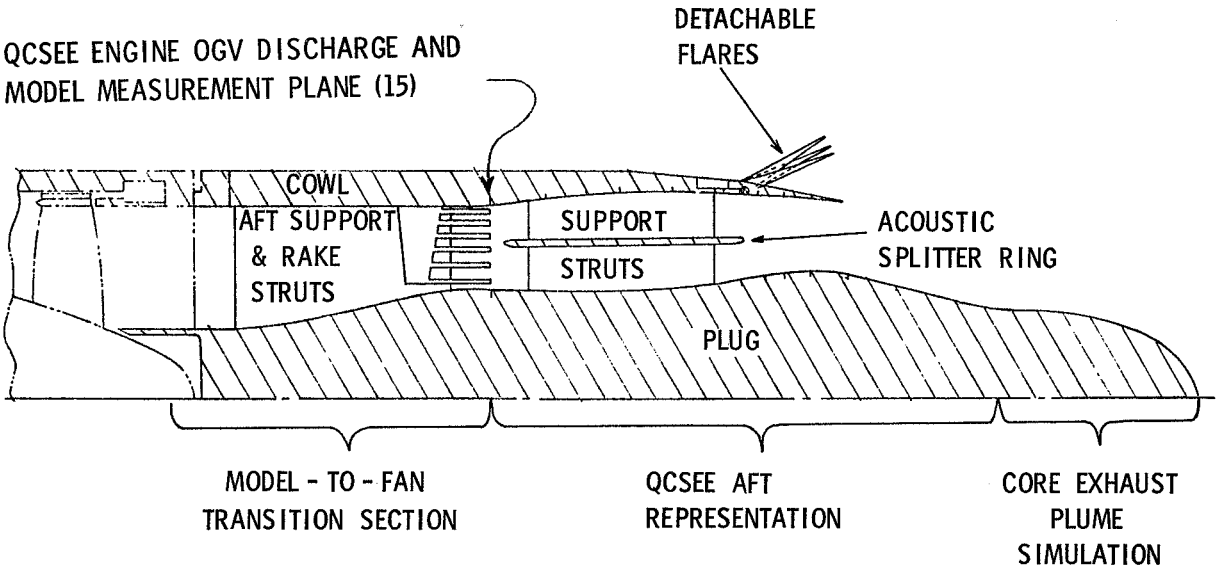

Figure 2. QCSEE 14 cm (5.5 in.) Exlet Model.

NASA
C-74-2718

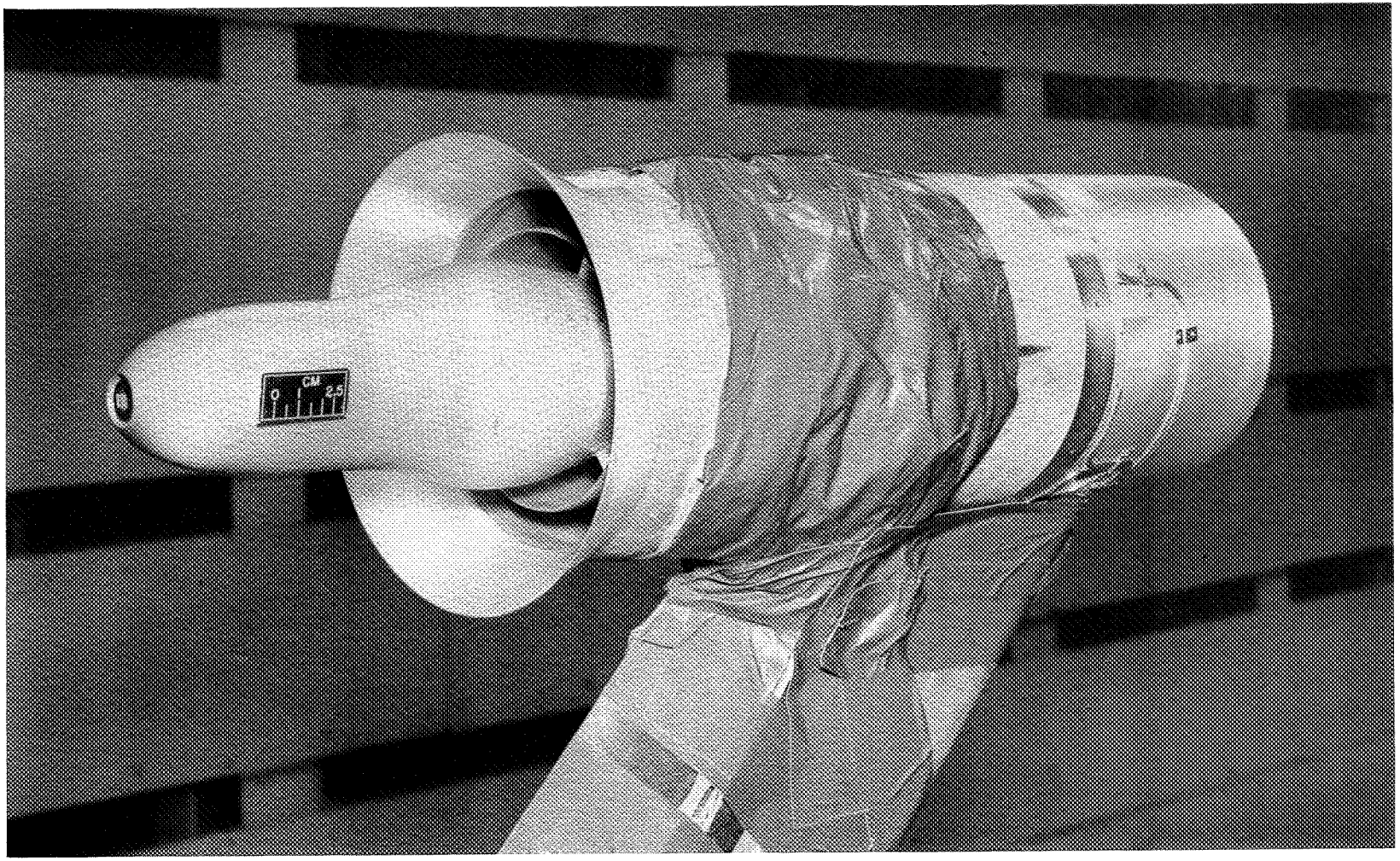

Figure 3. QCSEE 14 cm (5.5 in.) Exlet Model - Typical Tunnel Installation.

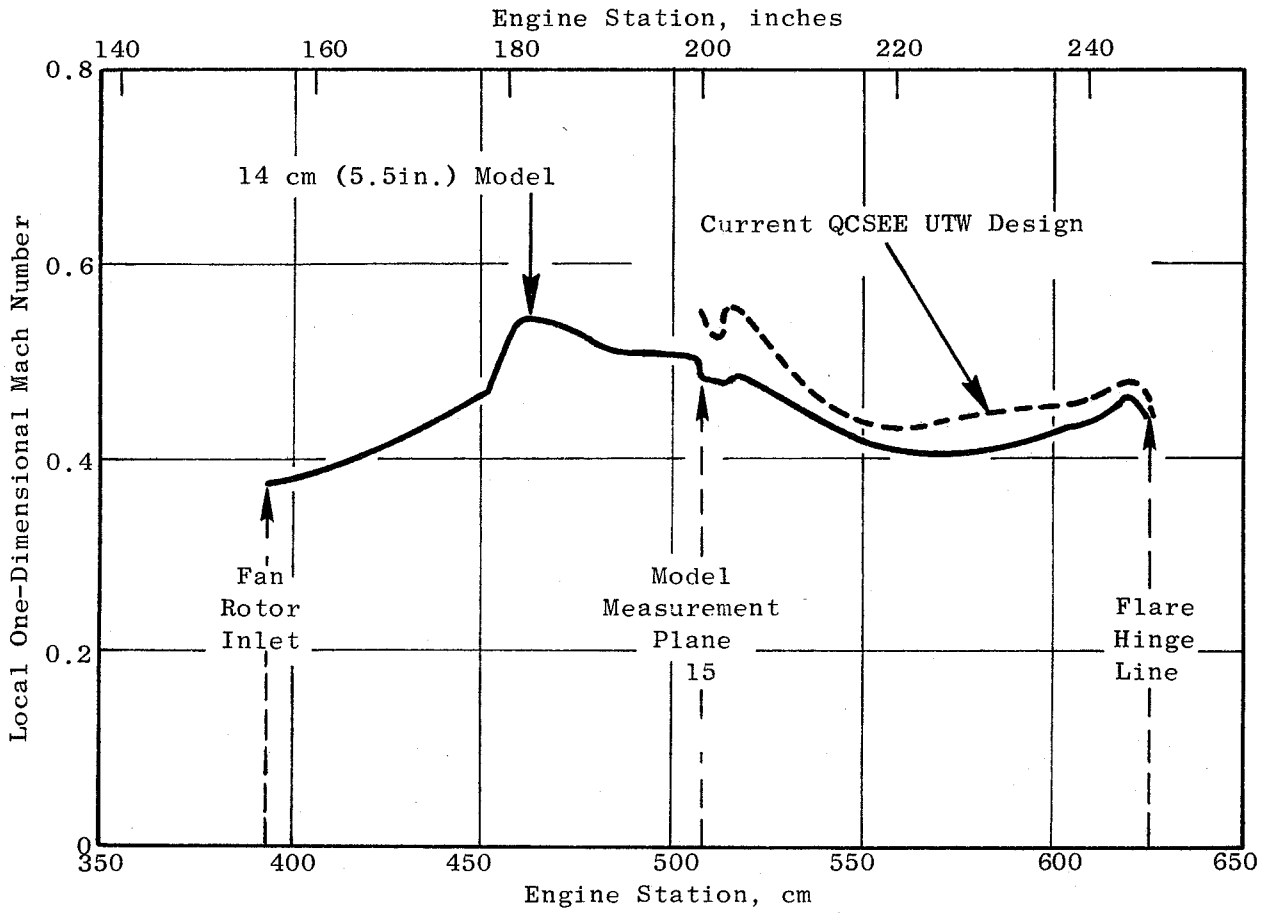

Figure 4. QCSEE Fan Duct Mach Number Distribution, Reverse-Thrust/Flow Operation.

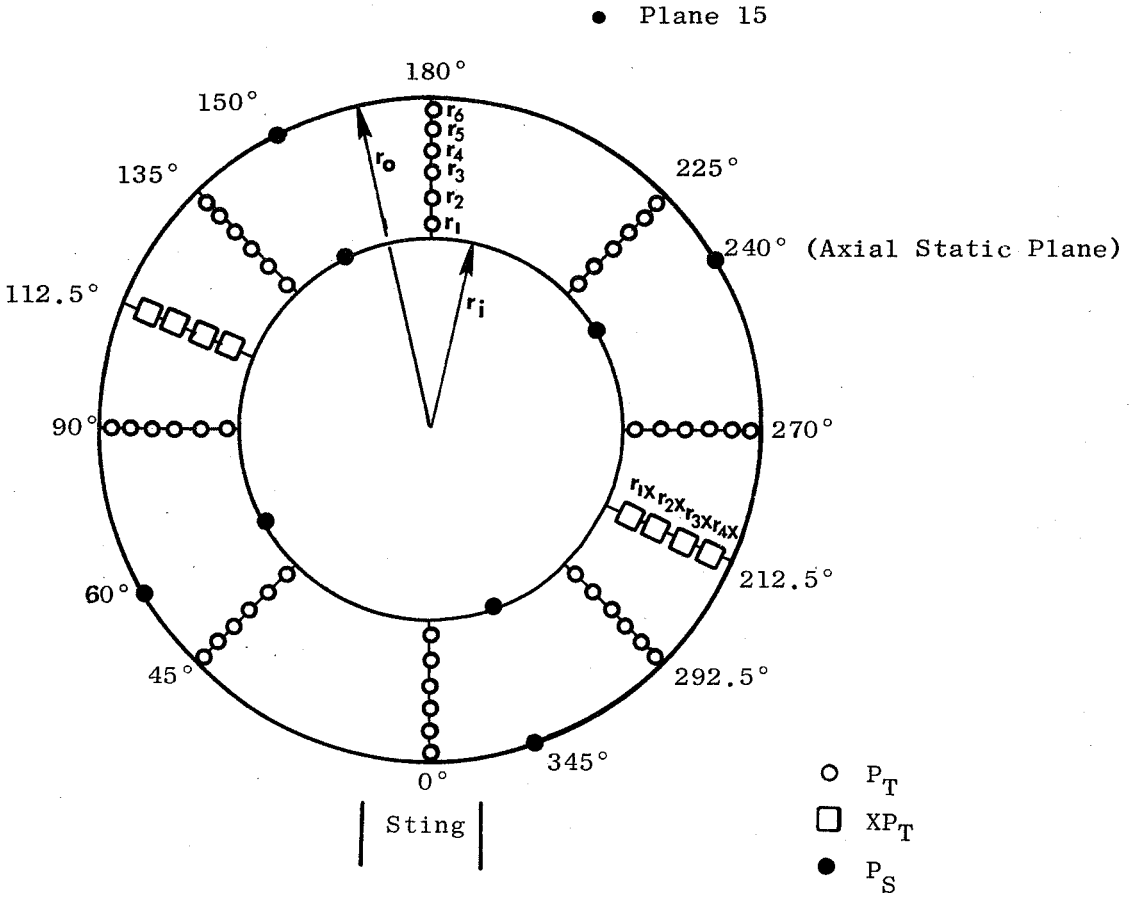

Radial dimensions - model annulus, and total pressure rakes.

r_i (Hub)	4.05 cm	(1.595 in.)	r_1	4.37 cm	(1.722 in.)
r_{1x}	4.30	(1.692)	r_2	4.95	(1.950)
r_{2x}	5.23	(2.061)	r_3	5.47	(2.155)
r_{3x}	5.97	(2.351)	r_4	5.95	(2.342)
r_{4x}	6.60	(2.598)	r_5	6.39	(2.515)
r_o (Tip)	7.00	(2.754)	r_6	6.80	(2.677)

Figure 5. Recovery/Distortion/Airflow Measurement Plane.

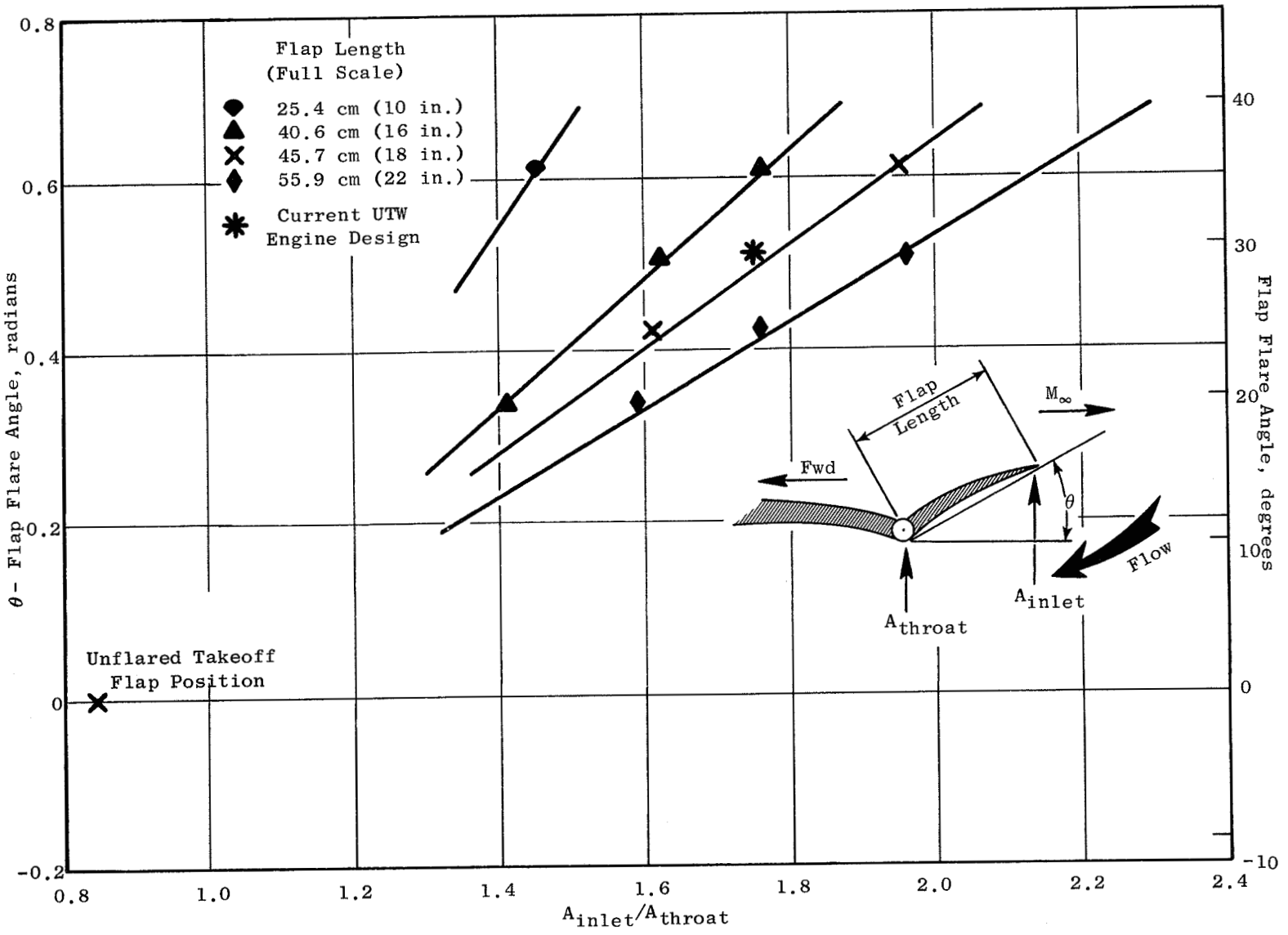

Figure 6. QCSEE Exlet Test Matrix.

was used as a performance reference and a vee-notched modification to the 45.7 cm (18 in.) flap/30° flare configuration to evaluate the effect of the major gaps between the nozzle leaves in the flare deployment configuration. This vee'd flare was also rotated relative to the basic instrumentation plane so as to provide evaluation of the vee-notch flow's direct impingement upon the dynamic pressure rakes as well as the steady-state total pressure rakes. Thus a total of 13 model flap/flare configurations were tested.

Each flare was evaluated in a matrix of four model flows spanning the scaled 180 to 360 kg/sec (400 to 800 lb/sec) QCSEE reverse-airflow range. These four airflows were obtained at the sea level static condition in addition to the four tunnel velocities: simulated landing speeds of approximately 80, 115, 160 and 240 km/hr (43, 62, 84 and 130 knots). Crosswind conditions, while not a QCSEE design requirement, were also evaluated by model rotation to a yaw angle that provided an approximate 65 km/hr (35 knot) velocity component normal to the nacelle. Crosswind effects were evaluated for all configurations.

4.0 DISCUSSION OF RESULTS

All data have been presented as a function of full-scale QCSEE reverse airflow by scaling the model airflow by a 166.64 factor which is the model scale factor squared. Current QCSEE engine estimate of maximum reverse-through-stall-pitch airflow is 254 kg/sec (560 lb/sec). Hereafter, this airflow level will be referred to as "maximum reverse airflow". Furthermore, the 45.7 cm (18 in.) 30° flare configuration will be referred to as the "base flare."

4.1 TOTAL PRESSURE RECOVERY

All flared configurations performed equivalently well as they provided a substantial performance benefit (0.035 to 0.05 increase in recovery in the 0 to 150 km/hr range) over the unflared configuration (Figure 7). Interpolated recovery values at the Maximum Reverse Airflow are presented as a function of simulated landing speed. Recovery for all the flared configurations did not vary more than 0.01 (i.e., data bandwidth) over a simulated landing speed range 0 to 240 km/hr. Typical flare recovery levels for 0 and 150 km/hr were 0.992 and 0.975 respectively, whereas the corresponding levels of the unflared configuration were about 0.958 and 0.925. Area ratios greater than 1.75 (base flare configuration) did not improve the recovery characteristic by any significant amount (~0.002) (see Figure 7). Increasing angle beyond 30° provided no benefit in recovery characteristics.

Recovery data for the selected base flare in the three configurations tested are presented in Figures 8 through 10; the unflared configurations recovery performance (Figure 11) is provided for improvement comparison. Recovery differences between the vee-notched and the rotated vee-notched base flare are attributable to the direct impingement of two of the vee notch wakes on the steady-state rakes for the nonrotated vee'd flare configuration. Crosswind data will be discussed in the "Crosswind Effects" section.

4.2 TOTAL PRESSURE DISTORTION

As would normally be expected of high recovery performance, distortion was low (Figures 12 and 13) in the 0 to 240 km/hr speed range investigated.

Circumferential distortion at maximum reverse airflow (Figure 12) was extremely low for flare configurations without vee-notches or crosswind. As shown in Figure 12, the IDC (Section 6.0, Nomenclature) values without crosswind generally fell in a range between 0.005 and 0.01, with exceptions showing values in the 0.014 to 0.019 range. A comparison of IDC values for the various flares shows the base configuration to have the lowest distortion. Circumferential distortion for unflared and vee-notched flare configurations showed some increase in IDC, with a peak value of 0.026 indicated. Crosswind effects upon distortion are covered in the last section.

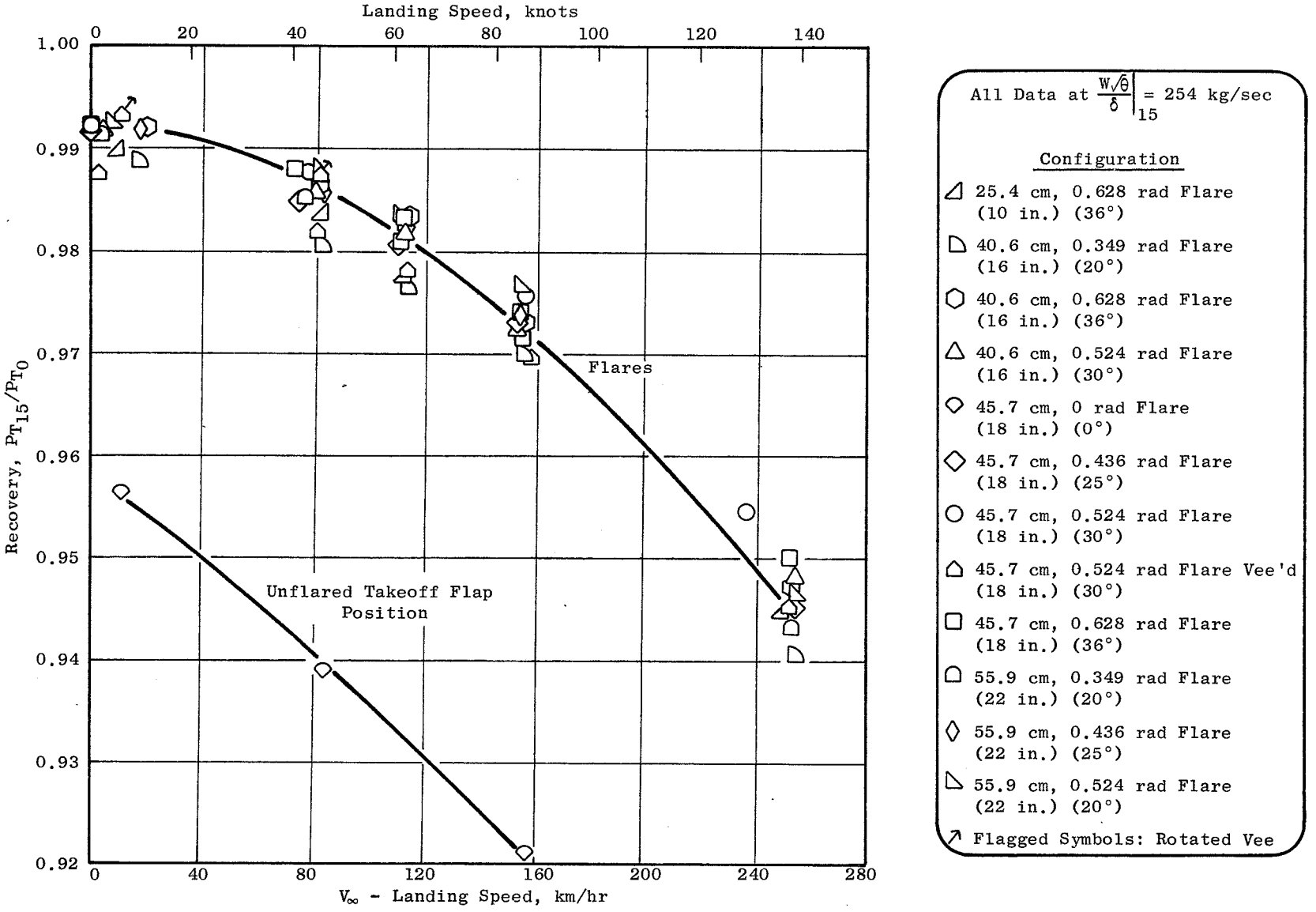

Figure 7. All-Flare Recovery Performance Summary.

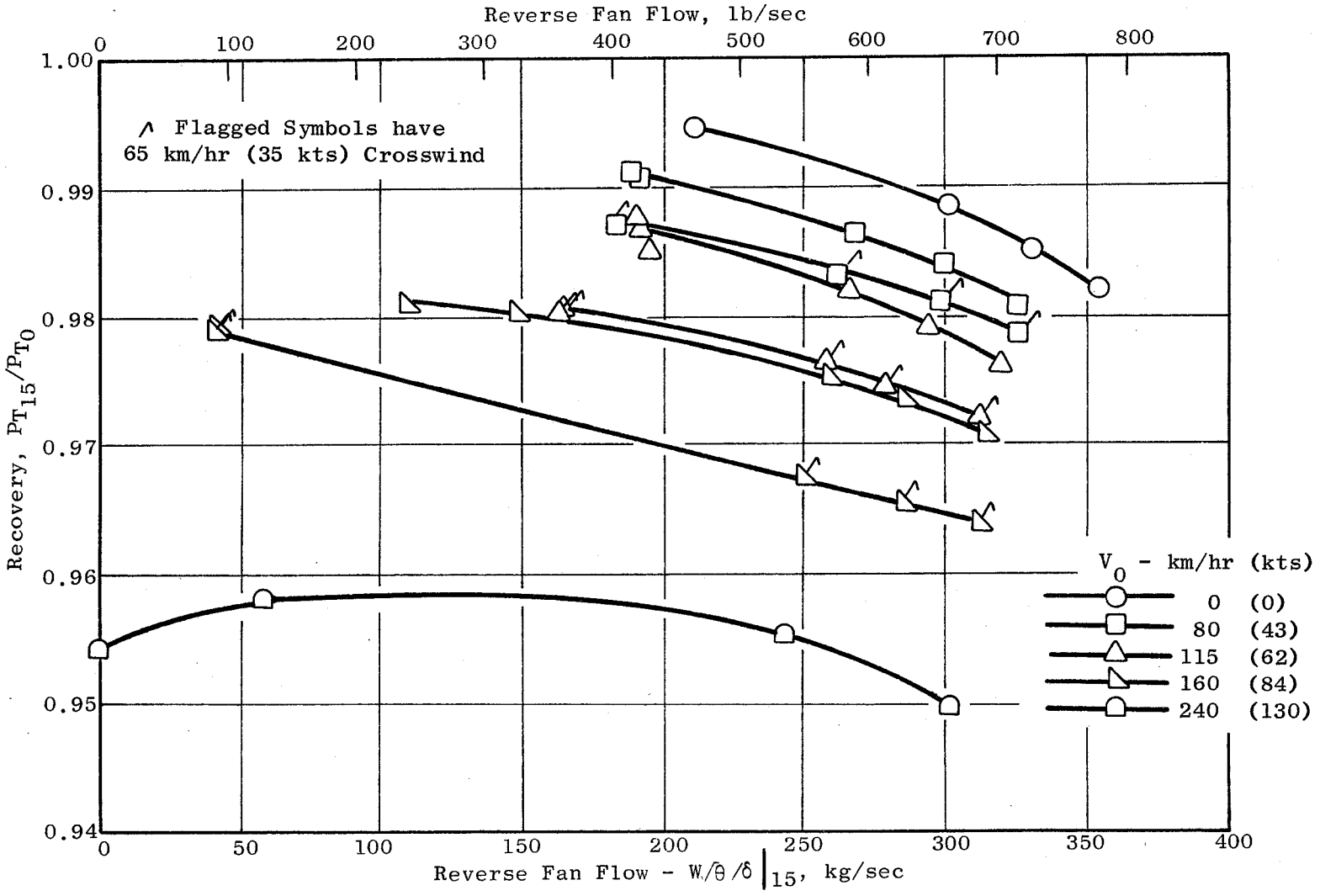

Figure 8. Recovery Characteristic with a Scaled 45.7 cm (18 in.) 30° Flare.

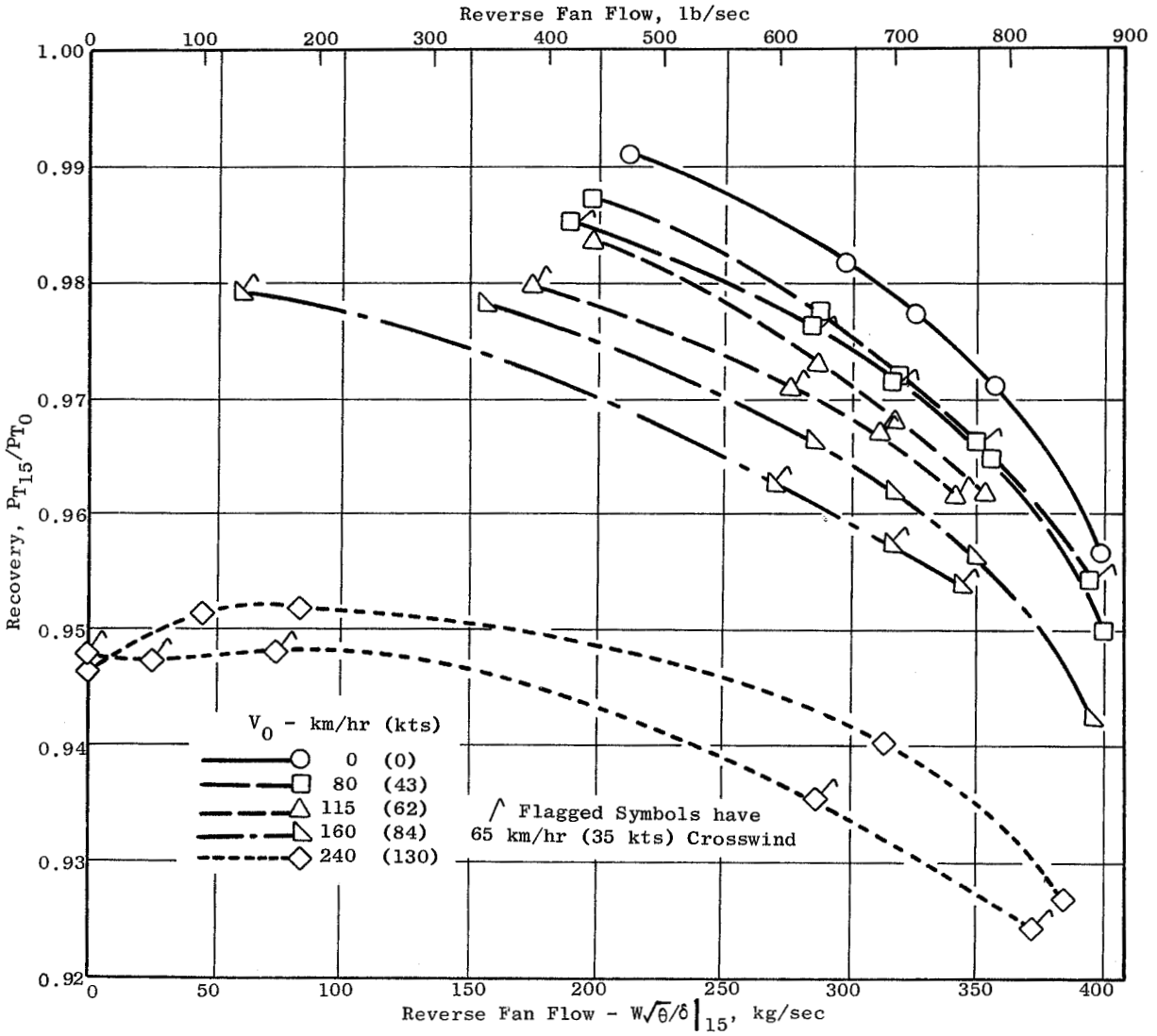

Figure 9. Recovery Characteristic with a Scaled Vee'd 45.7 cm (18 in.) 30° Flare.

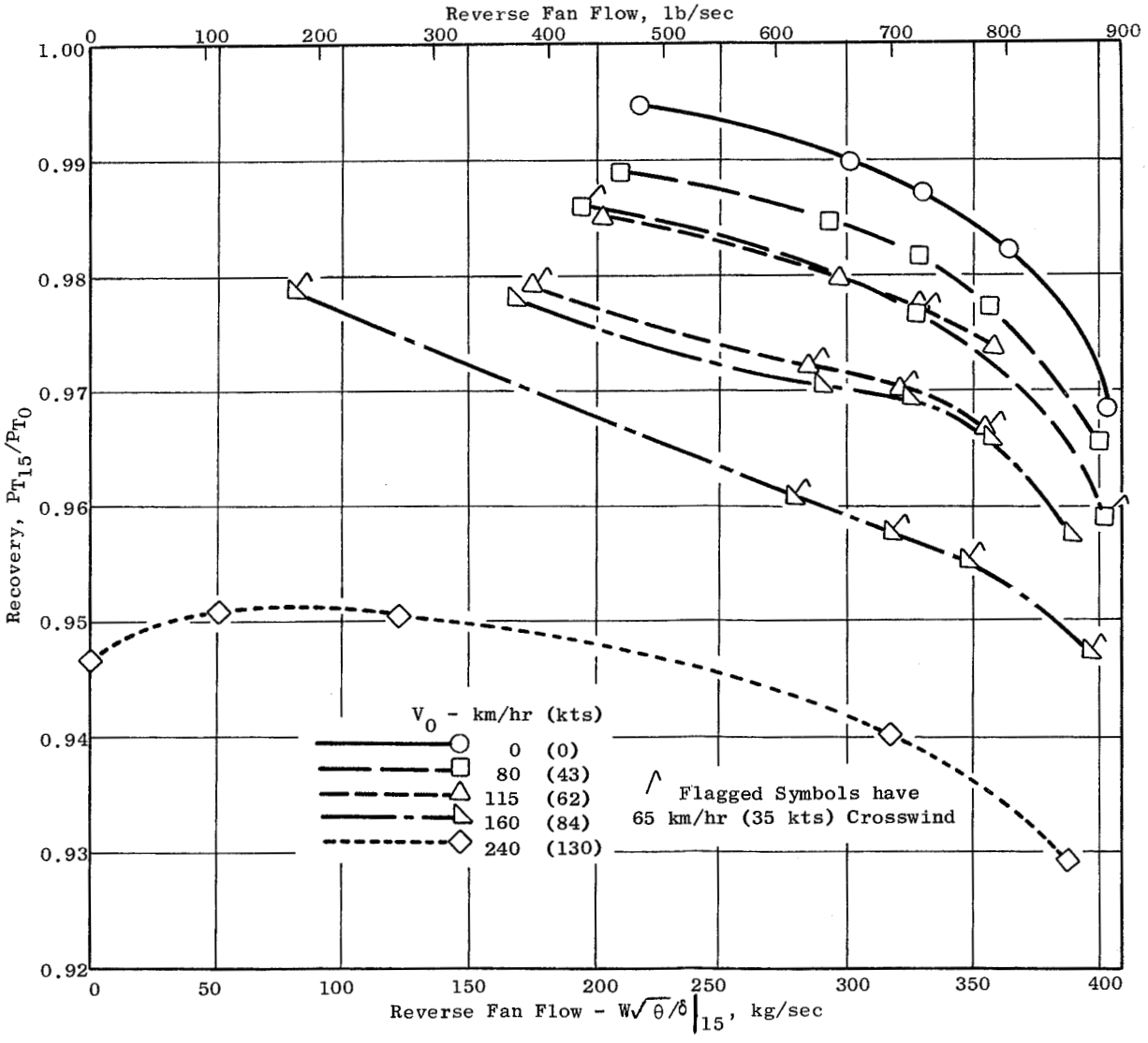

Figure 10. Recovery Characteristic with a Scaled Vee'd and Rotated $67\frac{1}{2}°$ 45.7 cm (18 in.) 30° Flare.

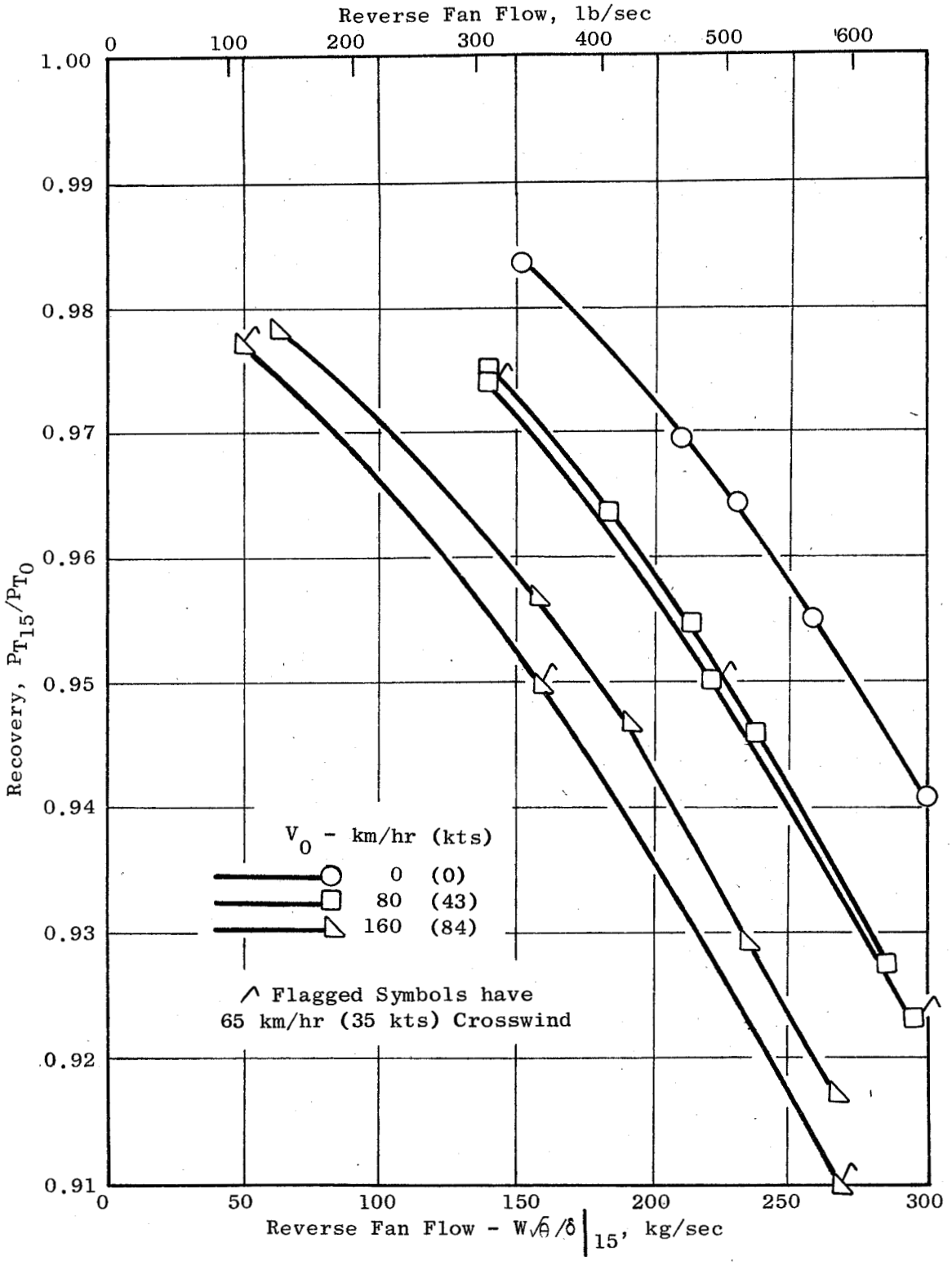

Figure 11. Recovery Characteristic with a Scaled 45.7 cm (18 in.) 0° Unflared Takeoff Flap Position.

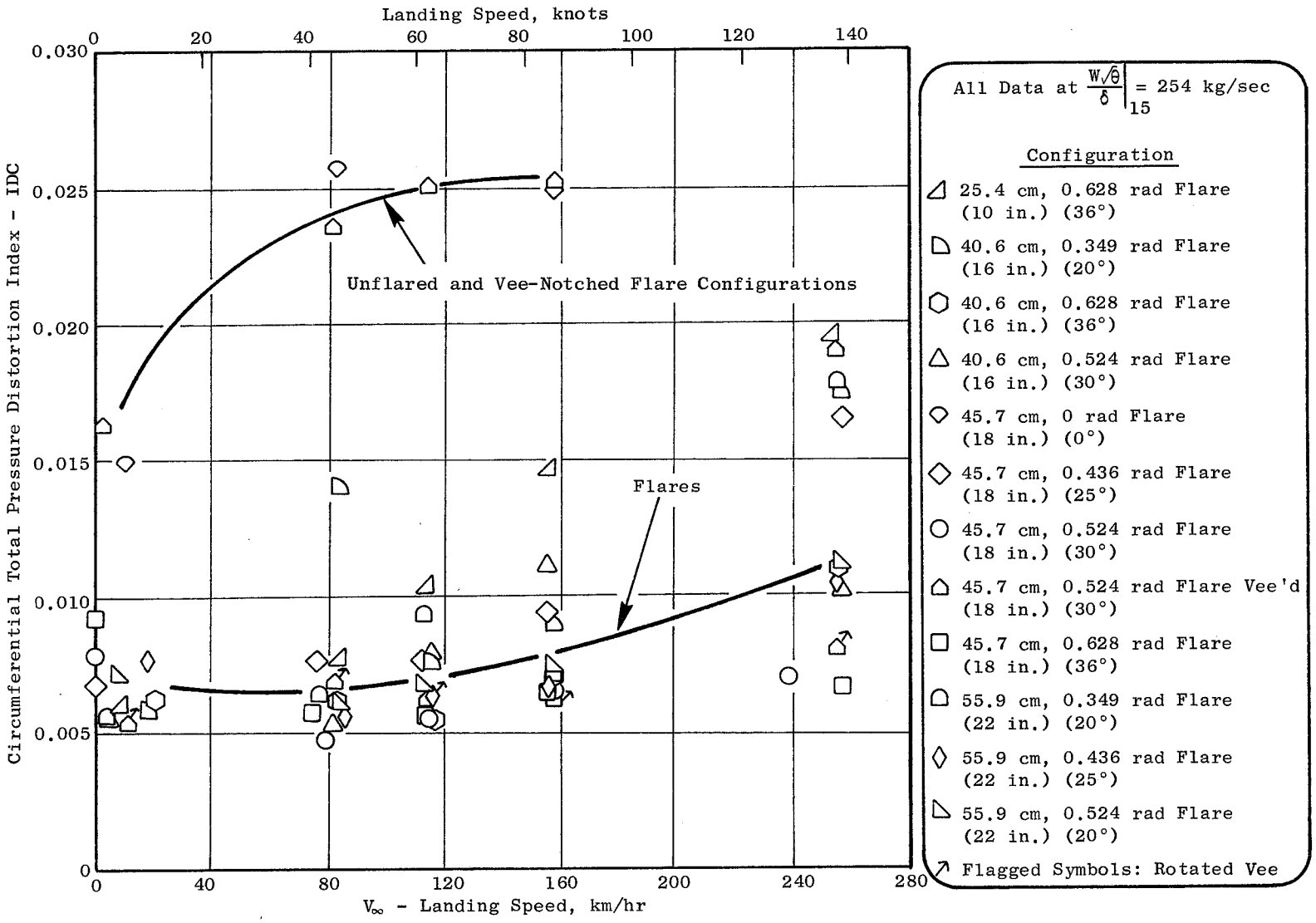

Figure 12. Circumferential Distortion Vs. Landing Speed.

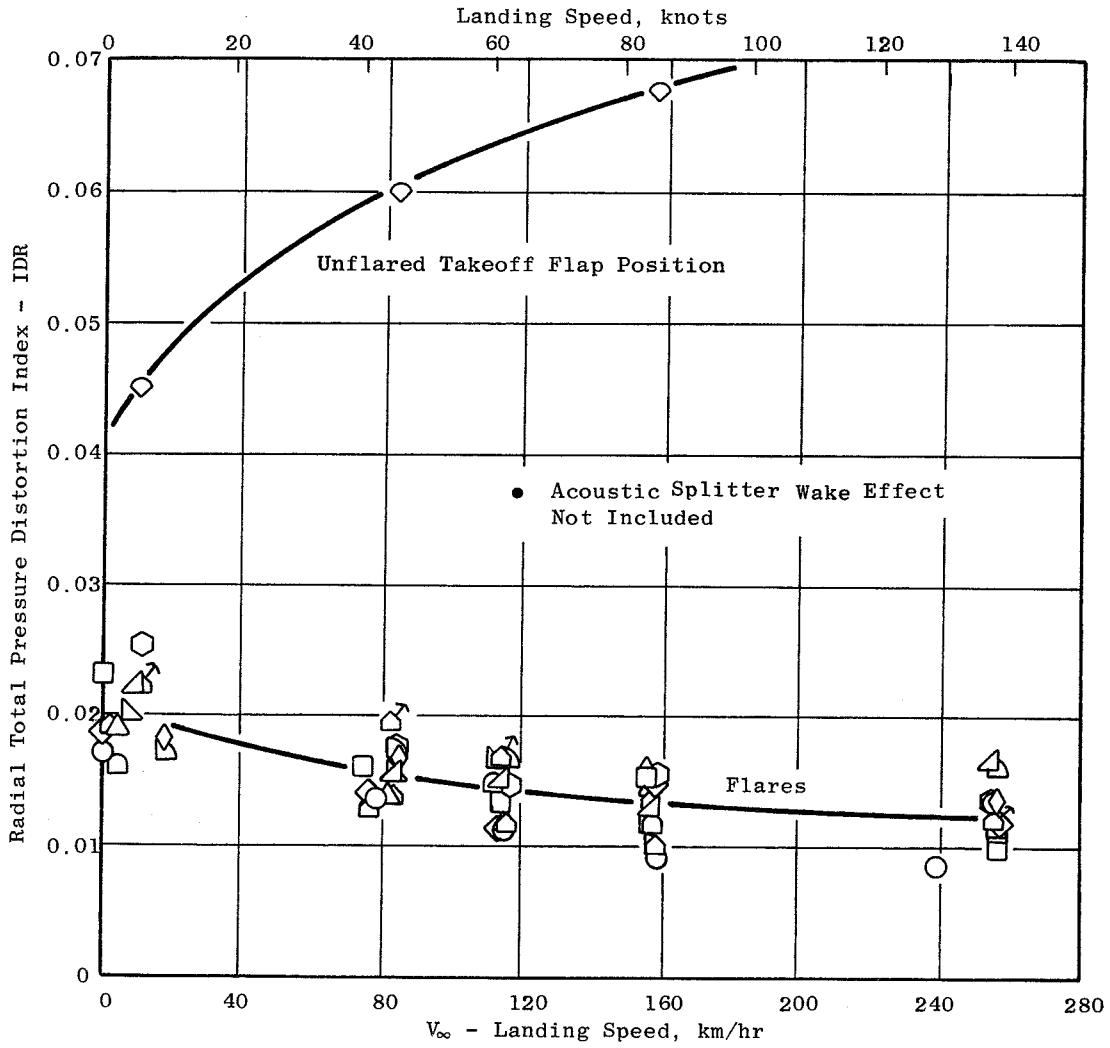

All Data at $\left.\frac{W\sqrt{\theta}}{\delta}\right|_{15}$ = 254 kg/sec

Configuration

- 25.4 cm, 0.628 rad Flare (10 in.) (36°)
- 40.6 cm, 0.349 rad Flare (16 in.) (20°)
- 40.6 cm, 0.628 rad Flare (16 in.) (36°)
- 40.6 cm, 0.524 rad Flare (16 in.) (30°)
- 45.7 cm, 0 rad Flare (18 in.) (0°)
- 45.7 cm, 0.436 rad Flare (18 in.) (25°)
- 45.7 cm, 0.524 rad Flare (18 in.) (30°)
- 45.7 cm, 0.524 rad Flare Vee'd (18 in.) (30°)
- 45.7 cm, 0.628 rad Flare (18 in.) (36°)
- 55.9 cm, 0.349 rad Flare (22 in.) (20°)
- 55.9 cm, 0.436 rad Flare (22 in.) (25°)
- 55.9 cm, 0.524 rad Flare (22 in.) (20°)
- ↗ Flagged Symbols: Rotated Vee

Figure 13. Radial Distortion Vs. Landing Speed.

The flare reduced the predominately radial distortion (Figure 13). The radial distortion index, IDR (Section 6.0, Nomenclature), ranged from 0.025 to 0.008 at the maximum reverse airflow for all the flared exlet configurations, while the unflared configuration varied from 0.045 to 0.068. Area ratios above 1.75 and flare angles above 30° did not reduce the distortion characteristics below those of the selected flare configuration.

As shown in Figure 13, there is a slight reduction of IDR with increasing landing speed for all flares. The decreasing IDR effect was a result of face average-pressure decreasing more rapidly than the minimum ring average pressure in the separated flow region. Rapid radial growth of the separated region's radial extent with increasing tunnel velocity was the primary cause. Another contributing factor was the decreasing hub recovery. The radial profiles in Figure 14 help to illustrate these effects. The agreement of inner and outer wall static average pressures indicates a good possibility of a flat radial static pressure profile. These profiles provide qualitative indication of the radial velocity profile. The unflared flap (Figure 15) has very poor agreement between the inner and outer wall statics, indicating a substantial velocity distortion with a higher velocity in the hub region. Thus, the flare exlet provides a more uniform velocity profile.

Because of the acoustic splitter wake and the six rings of probes at the measurement plane, the definition of IDR used herein differs slightly from the standard General Electric distortion methodology definition. The maximum IDR value of only five of the six rings was used. The third-radius ring IDR was omitted because it had little variability among the various flare configurations since it was always the highest of the 6-ring IDR values; that ring was partially immersed in the acoustic splitter wake, which was a small radial-extent pressure defect of an estimated peak-value IDR of approximately 0.07 at maximum reverse airflow. Hence the 3rd-ring IDR precluded detection of radial distortion effects by the various flare configurations.

Figures 16 and 17 show the excellent low radial distortion vs. airflow characteristic of the base flare configuration, while Figure 18 shows the high radial distortion of the unflared flap setting.

4.3 TOTAL PRESSURE FLUCTUATION

Waveforms of the eight dynamic total pressure measurements were obtained by oscillograph traces recorded on-line. These on-line observations indicated the flare exlets reduced pressure fluctuation levels by 2/3 from the unflared configuration. The inner flowpath (hub region) showed quite low-level activity, about 1% ΔPRMS/P for all flare exlets. The outer flowpath (tip region) of the flare exlets had about the same low fluctuation level up to around 225 kg/sec (500 lb/sec). As airflow increased, an intermittent separation which was not circumferentially uniform, produced alternating pressure fluctuations levels of about 1% and 2-1/2% ΔPRMS/P. Individual probes at opposing circumferential locations exhibited this through an out-of-phase

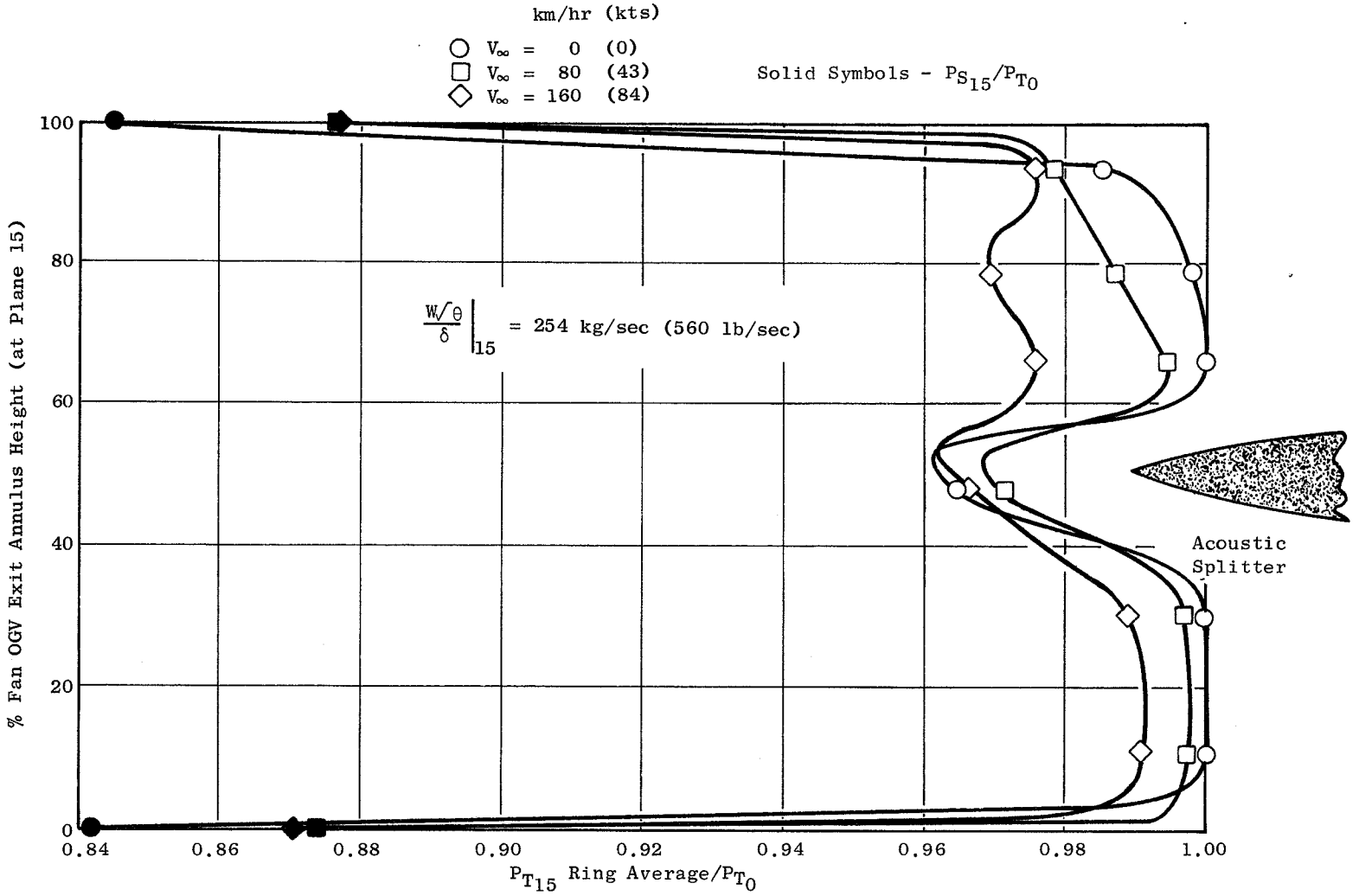

Figure 14. Radial Total Pressure Profiles at QCSEE 254 kg/sec (560 lb/sec) Airflow - Effect of Forward Velocity.

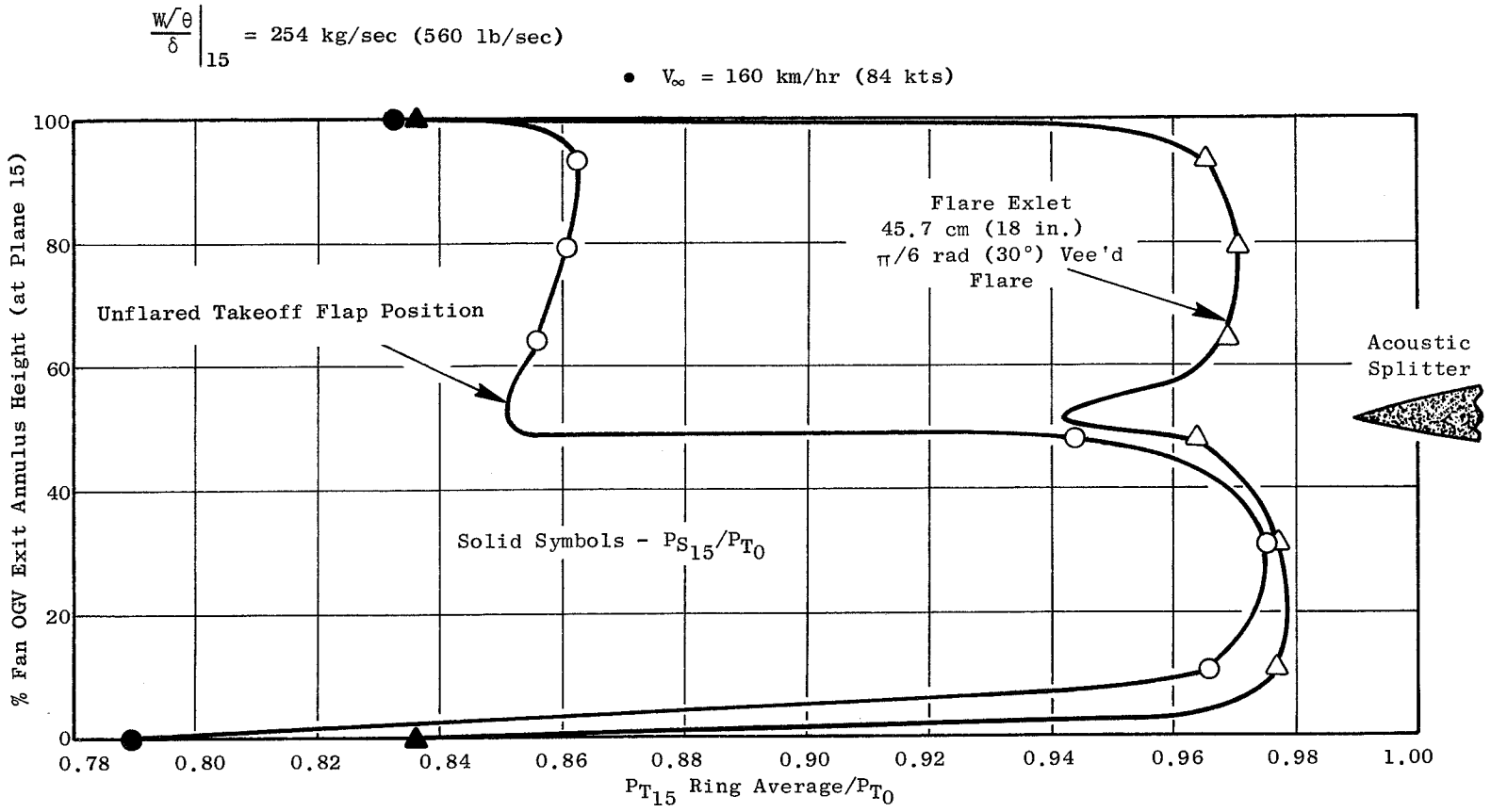

Figure 15. Radial Total Pressure Profiles at QCSEE 254 kg/sec (560 lb/sec) Airflow.

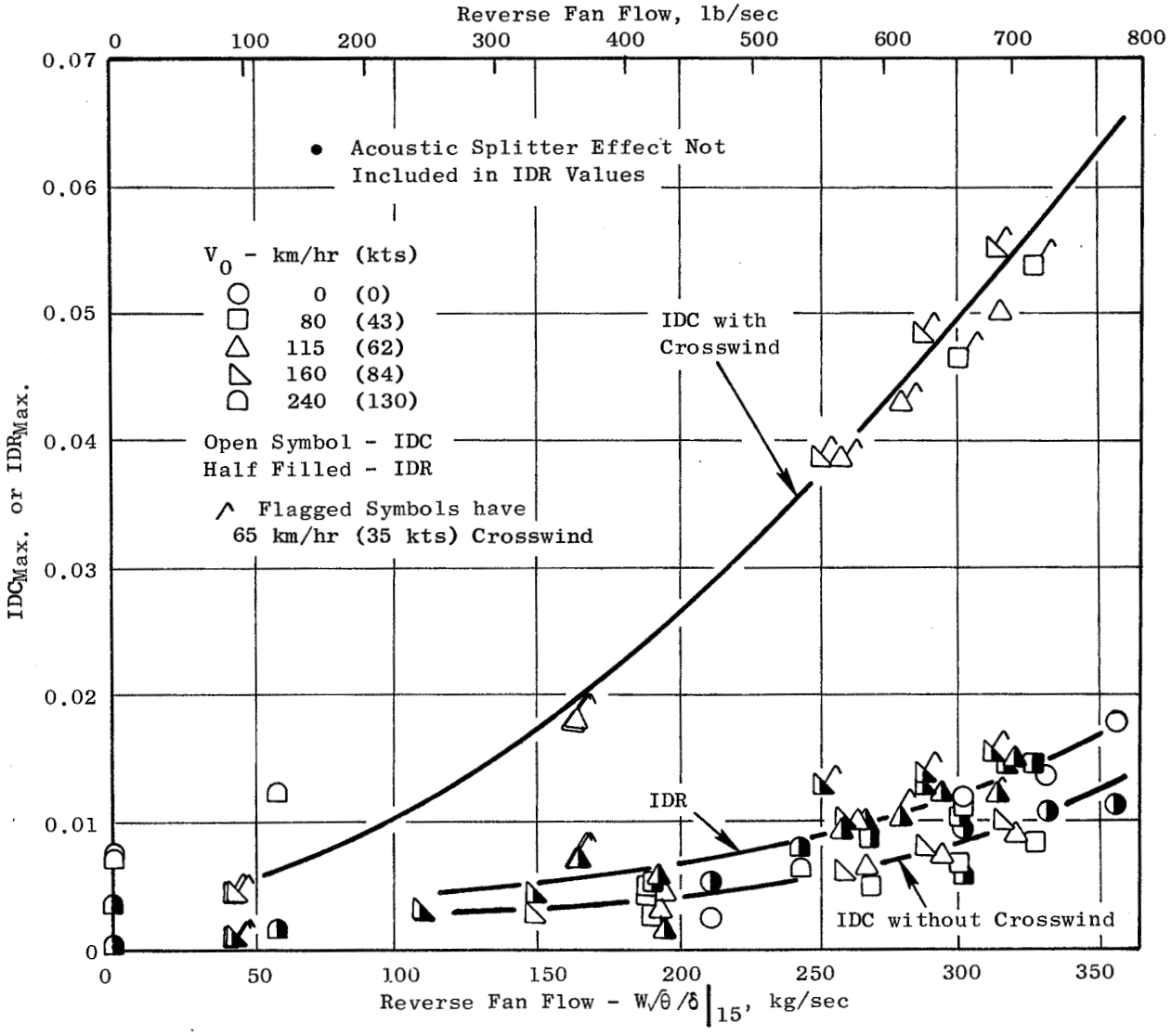

Figure 16. Distortion Characteristics with a Scaled 45.7 cm (18 in.) 30° Flare.

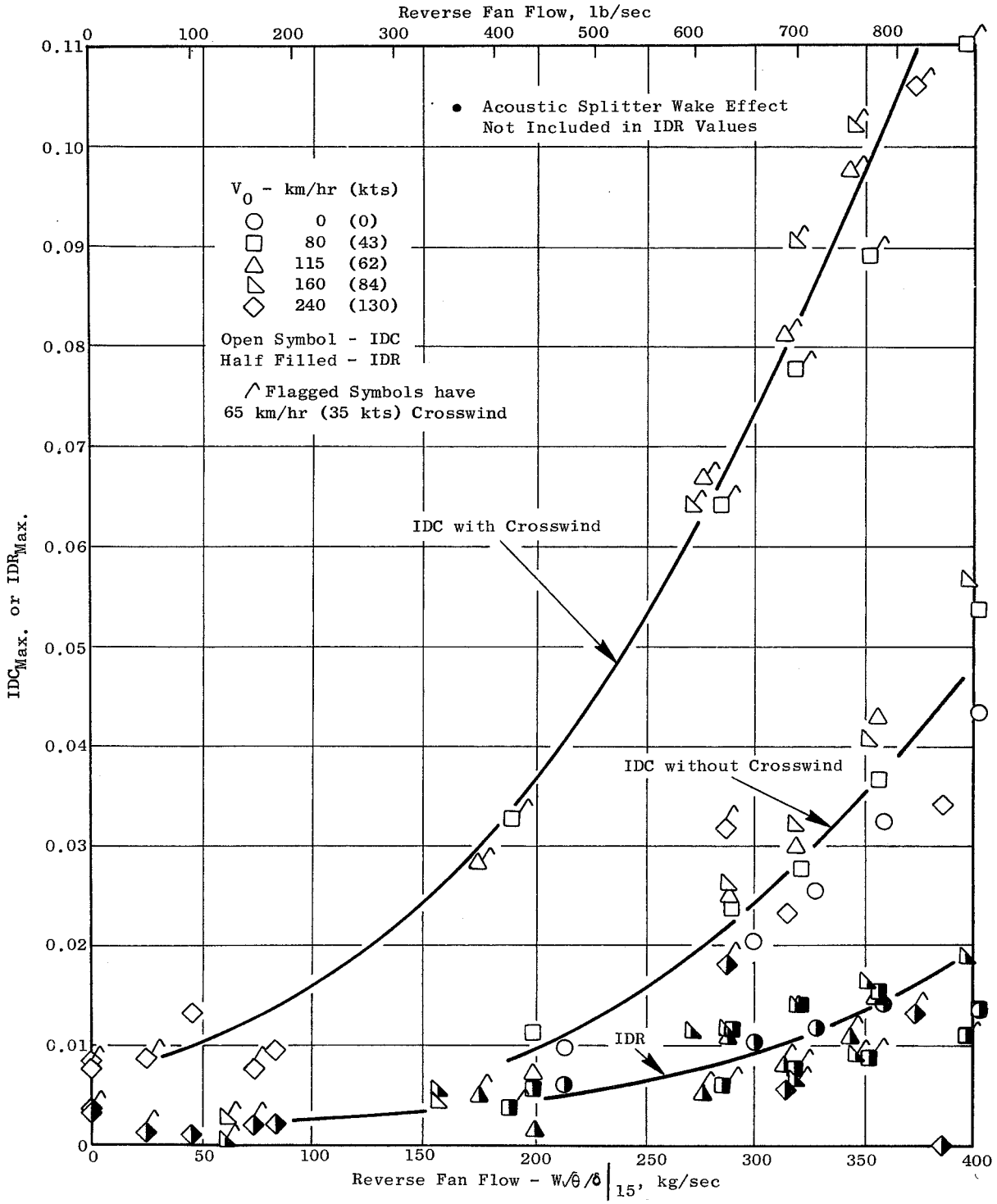

Figure 17. Distortion Characteristics with a Scaled Vee'd 45.7 cm (18 in.) 30° Flare.

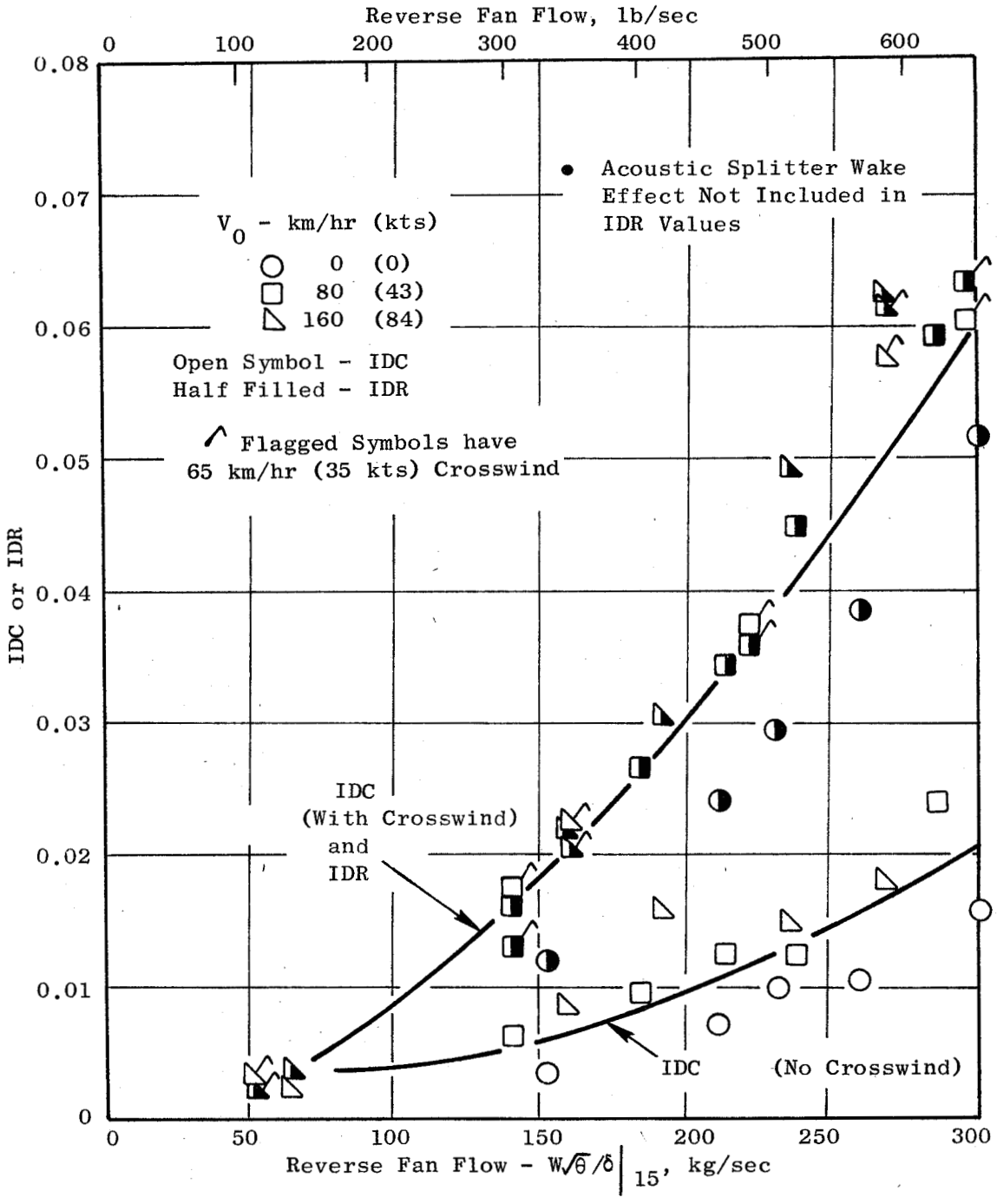

Figure 18. Distortion Characteristics with a Scaled 45.7 cm (18 in.) 0° Unflared Takeoff Flap Position.

pressure fluctuation which was accompanied by an alternating temporal-mean ("steady-state") level of pressure. Previous inlet tests, for which dynamic distortions were calculated, exhibited dynamic distortion levels 3 to 4 times the steady-state level in the regions of intermittent separation (reference 2). Dynamic distortions could not be obtained on this test because of insufficient dynamic instrumentation. At the higher airflows, about 295 kg/sec (650 lb/sec), the separation phenomena stabilizes into more homogeneous turbulence of moderate level (as indicated by pressure fluctuations of about 2%), which reduces the ratio of dynamic-to-steady-state distortion levels previously mentioned.

4.4 VEE-NOTCHED EFFECT

Four small vee notches were cut in the base flare configuration to simulate the open area between the nozzle flap leaves in the deployed flare configuration (see Figure 19). These notches resulted in a recovery loss of less than 0.01 based on results of the two vee'd flare rotation positions (Figures 8, 9 and 10).

The vee notches had no noticeable effect upon radial distortion. Furthermore, vee notching changed the distortion pattern from a predominately radial to a combined circumferential and radial pattern (Figures 20 and 21). Shear phenomena at the vee notches generated small-extent regions of even lower pressure at the tip which increased the circumferential distortion (Figures 16 and 17). At the maximum reverse airflow (254 kg/sec) the increase was about 0.01, while at the upper limit of airflow investigated (360 kg/sec) the increase in circumferential distortion was about 0.025. These extra deficiencies in the tip region were accompanied by a local increase of turbulence level as indicated by a 20% increase in dynamic total pressure fluctuations.

4.5 CROSSWIND EFFECTS

At four tunnel velocities, the model was yawed to obtain an approximate 65 km/hr component of velocity normal to the model centerline. Although crosswind effects was not a QCSEE design requirement, considerable data were obtained.

Crosswind had a degrading effect upon flare exlet performance (Figures 16, 17, and 18), primarily through an increase in circumferential distortion. At maximum reverse airflow the IDC increases ranged from about 0.035 to 0.05. The circumferential distortion increase was accompanied by a recovery decrease; for instance, from Figures 8, 9, and 10, typical losses at maximum reverse airflow were less than 0.01, and flow separation was noticed at much lower airflows. Radial distortion was essentially unaffected (ΔIDR $\approx$0.01).

Crosswind changed the distortion pattern shape by deepening the windward tip low pressure region and creating a new low pressure region in the hub on the leeward side of the model plug (Figure 22). The new hub distortion was accompanied by a turbulence increase in that region.

NASA
C-74-2725

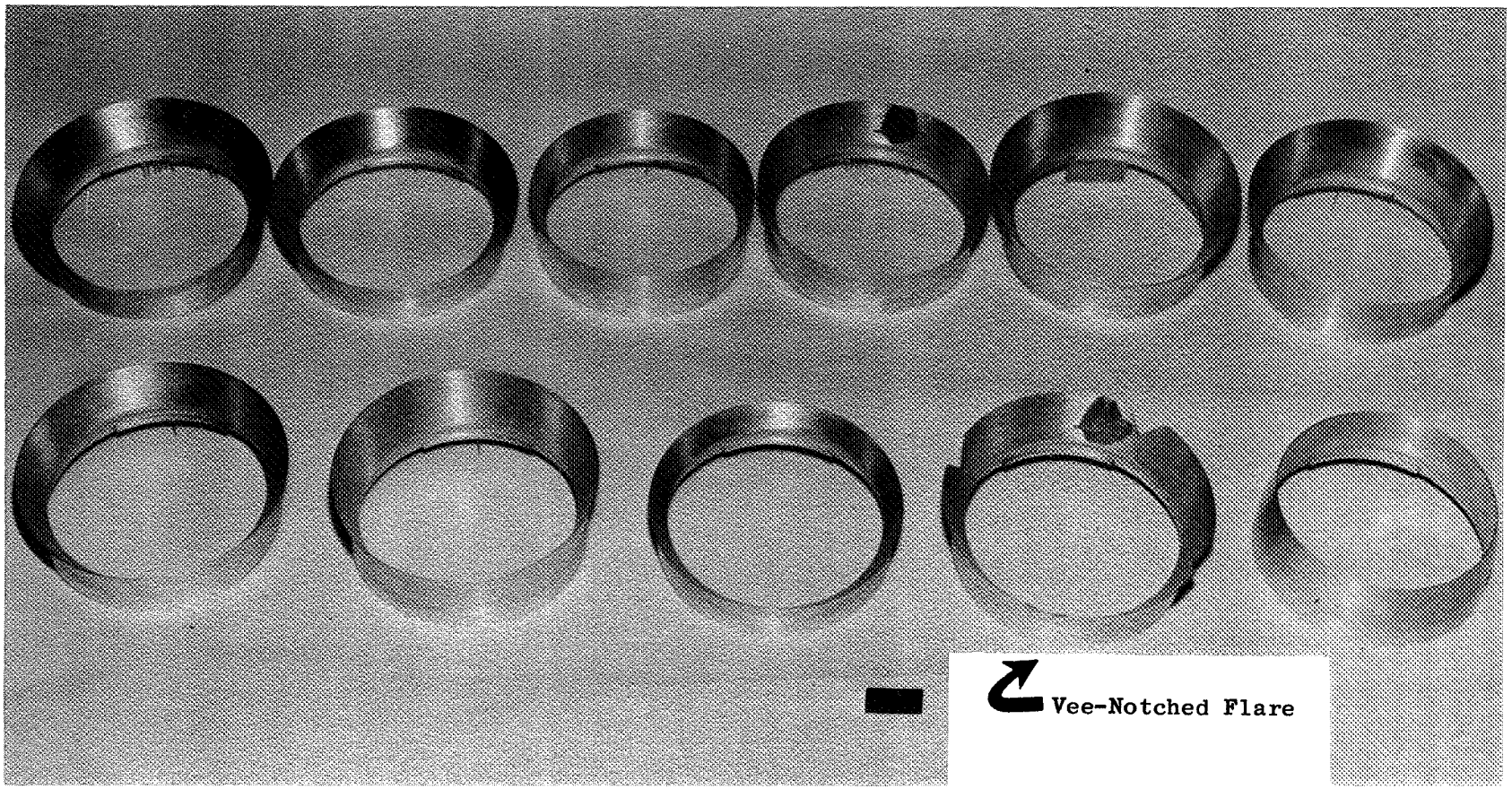

Figure 19. Array of Tested Detachable Flares.

- Configuration "A"
- 45.7 cm (18 in.) Flap,
- $\pi/6$ rad (30°) Flare

- V_0 = 159 km/hr. (85.8 knots)
- $\left.\frac{W\sqrt{\theta}}{\delta}\right|_{hs}$ = 259 kg/sec (571 lb/sec)
- No Crosswind

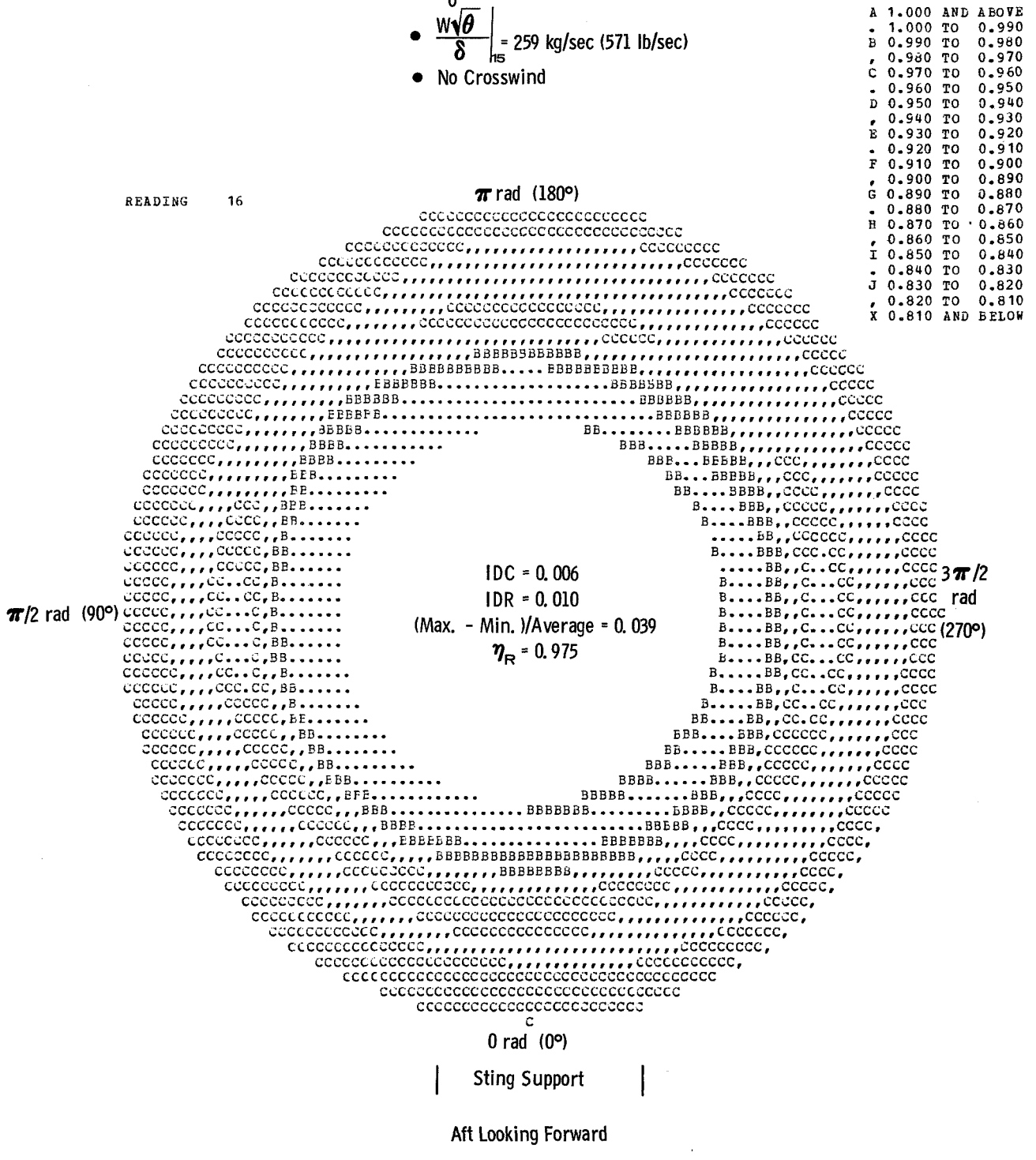

Figure 20. Total Pressure Contour Map at OGV Exit; a Scaled 45.7 cm (18 in.) 30° Flare.

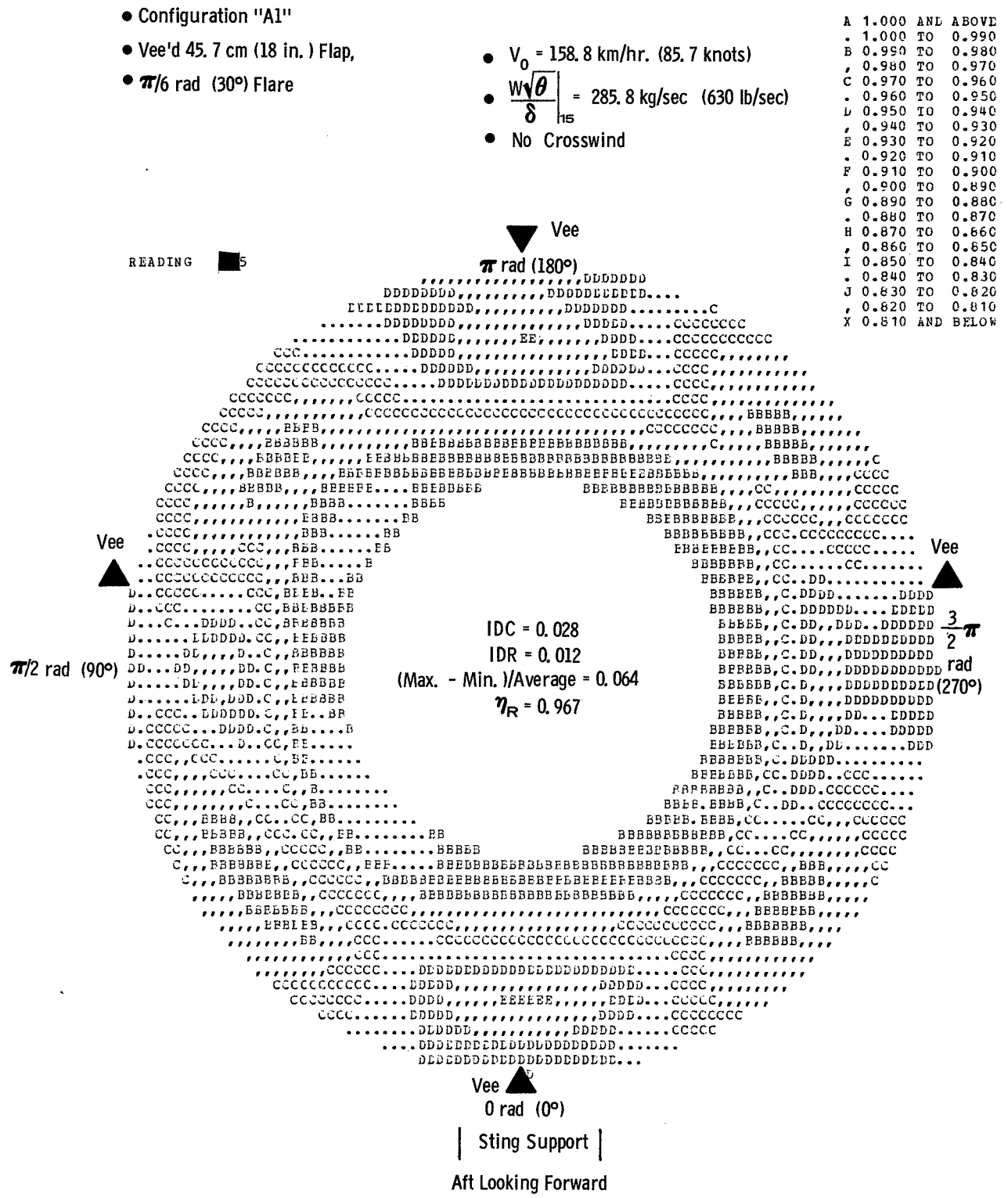

Figure 21. Total Pressure Contour Map at OGV Exit; a Scaled Vee'd 45.7 cm (18 in.) 30° Flare.

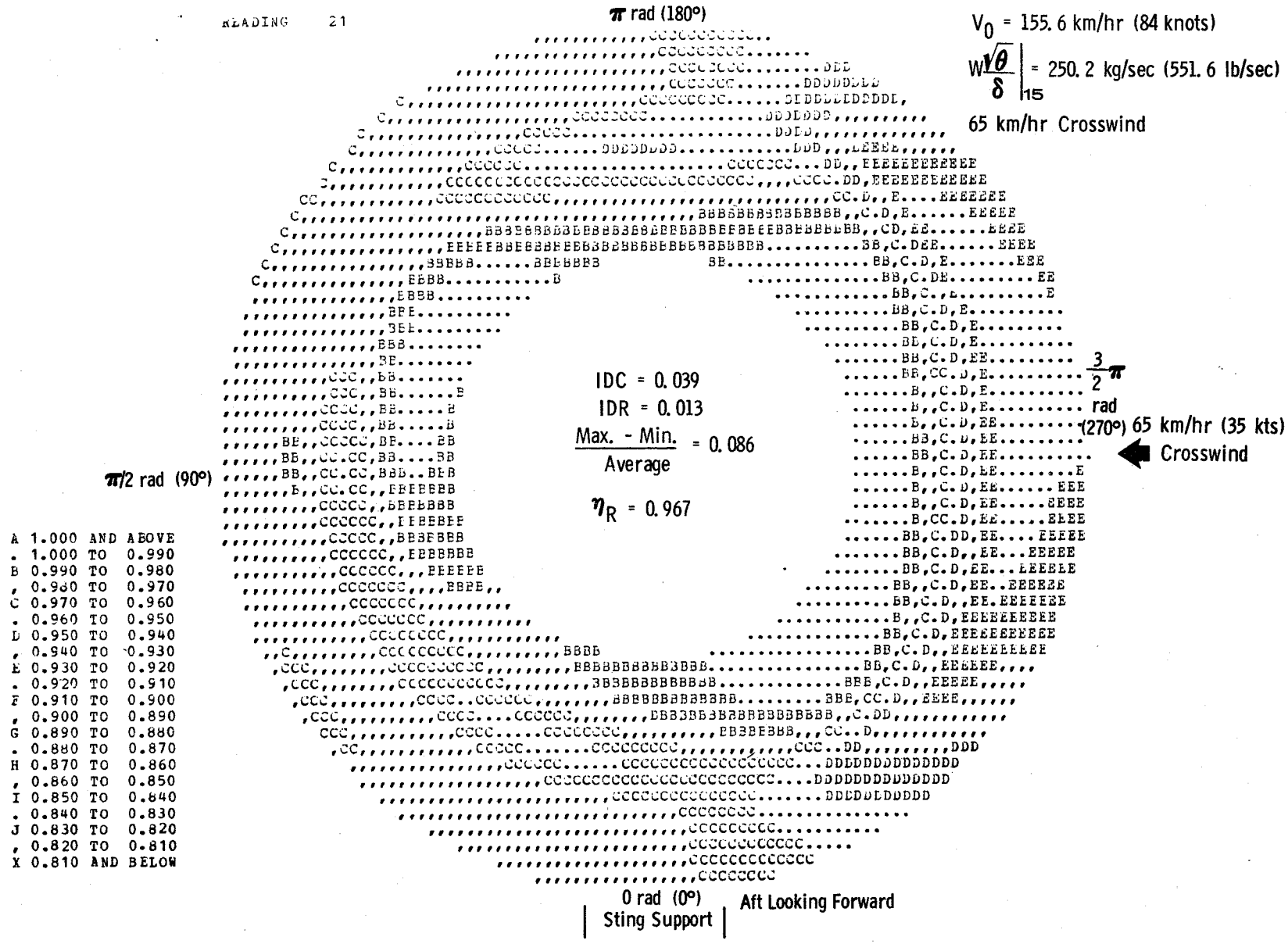

Figure 22. Total Pressure Contour Map at OGV Exit with Crosswind; a Scaled 45.7 cm (18 in.) 30° Flare.

The vee-notched flare configuration was affected by crosswind by an additional recovery decrease of about 0.005 and an additional circumferential distortion (IDC) increase of about 0.04. This model configuration with crosswind produced the test's highest distortions (refer to Figure 17).

5.0 CONCLUSIONS

Wind tunnel tests of scale model QCSEE variable pitch fan thrust reverser inlets were conducted to determine pressure recovery and distortion levels for a range of simulated engine airflows and landing speeds. These reverser inlets were formed by flaring the QCSEE engine variable fan nozzle flaps outward for improved reverse flow characteristics by way of a larger entrance area. Conclusions drawn from these data are:

- The flared nozzle is an acceptable reverser inlet concept for the QCSEE variable pitch fan engine.

- The flared nozzle concept provides substantially better reverse mode inlet recovery compared to the unflared nozzle position. Improvements of 0.035 to 0.05 were observed in a landing speed range from 20 to 150 km/hr.

- The flared nozzle concept provides low inlet distortion relative to the unflared takeoff nozzle position. Radial distortion indices at simulated maximum engine reverse airflow conditions ranged from 0.01 to 0.025 compared to 0.04 to 0.07 for the unflared case.

- The 45.7 cm (full scale) 30° flare configuration selected for the QCSEE variable pitch fan engine reverser inlet proved to be the best configuration. It provided the highest inlet recovery with the lowest distortion level of all the flares investigated.

6.0 NOMENCLATURE

A_{inlet}/A_{throat} = flare internal contraction ratio based upon the plane, annular, cross section areas

IDC = maximum of IDC_{tip} or IDC_{hub} = Circumferential Distortion index (total pressure at measurement plane)

$IDC_{hub} = \frac{1}{3} \sum_{i=1}^{3} IDC_{ring(i)}$

$IDC_{tip} = \frac{1}{3} \sum_{i=4}^{6} IDC_{ring(i)}$

$IDC_{ring} = \frac{\text{Ring Average - Ring Minimum}}{\text{Face Average}}$, each of 6 rings

where: i = 1 is ring at smallest radius
i = 6 is ring at largest radius

IDR = maximum of IDR_{ring} (i=3 ring excluded, see pg 20) = Radial Distortion Index (total pressure at measurement plane)

$IDR_{ring} = \frac{\text{Face Average - Ring Average}}{\text{Face Average}}$, each of 6 rings

where i = 1 is ring at smallest radius
i = 6 is ring at largest radius

$\frac{\text{Max. - Min.}}{\text{Average}} = \frac{\text{(Face Max. - Face Min.)}}{\text{Face Average}}$ = Face Distortion Index (total pressure at measurement plane)

P_s = exlet wall static pressure

P_T = exlet steady state total pressure in plane 15

XP_T = exlet dynamic (fluctuating) total pressure in plane 15

$\Delta PRMS/P$ = Root mean square pressure fluctuation divided by the temporal average pressure

P_{T_o} = wind tunnel total pressure

$P_{s_{15}}$ = measurement plane 15 static pressure

$P_{T_{15}}$ = measurement plane 15 total pressure

V_o = tunnel test section velocity

V_∞ = simulated aircraft landing speed

$$V_\infty = V_o \cos \alpha$$

where α = model yaw angle

$\left.\frac{W\sqrt{\theta}}{\delta}\right|_{15}$ = corrected exlet model fan flow scaled to total QCSEE engine reversed airflow, as measured by the measuring plane average static and average total pressures

η_R = exlet total pressure recovery measurement plane = $P_{T_{15}}/P_{T_o}$

7.0 REFERENCES

1. Keith, T.G.; "Subsonic Flow into a Downstream Facing Inlet", AIAA Journal of Aircraft, Vol. II, No. 4, April 1974, pp. 251 - 252.

2. Jones, J.R. and Douglass, W.M. (Douglas Aircraft Co.); "Dynamic Flow in Engine Air Inlets for Subsonic Aircraft", Project Squid - Proceedings of a Workshop held at Georgia Institute of Technology 6/10-11/71 sponsored by Purdue University, Lafayette, Indiana. Page 1.

DISTRIBUTION LIST

AiResearch Division
Garret Corporation
F.B. Wallace
402 South 36 Street
Phoenix, Arizona 80434

American Airlines
Maintenance and Engineering Center
K. Grayson
Tulsa, Oklahoma 74151

Andrews Air Force Base
Lt. Col. G. Strand
AFSC Headquarters
Washington, D.C. 20334

AVCO/Lycoming
S. Deckert
550 S. Main Street
Stratford, Connecticut 06497

The Boeing Company
H. Higgins
P.O. Box 3999
Seattle, Washington 98124

The Boeing Company
Wichita Division
D. Torkelson
Wichita, Kansas 67210

Bolt, Beranek and Newman, Inc.
R. Hayden
50 Moulton Street
Cambridge, Massachusetts 02138

Curtiss-Wright Corporation
Power Systems Division
W. Johnson
One Passaic Street
Wood Ridge, New Jersey 07075

Department of Transportation
NASA/DOT Joint Office of Noise Abatement
C. Foster
Office of Secretary
Washington, D. C. 20590

Detroit Diesel Allison Division of General Motors
F. Walters
Suite 312
333 West First Street
Dayton, Ohio 45402

Douglas Aircraft Company
L. Malthan
3855 Lakewood Boulevard
Long Beach, California 90801

Enivronment Protection Agency
J. Schettino
1835 "K" Street, NW
Washington, D.C. 20460

Federal Aviation Administration
Noise Abatement Division
J. Woodall
Washington, D.C. 20590

General Dynamics Convair Division
G. Nicoloff
San Diego, California 92112

Grumman Aerospace Corporation
C. Hoeltzer
South Oyster Bay Road
Bethpage, New York 11714

Hamilton Standard
Division of United Aircraft
A. Jackson
Windsor Locks, Connecticut 06096

Lockheed Aircraft Corporation
T. Higgins
Burbank, California 91503

Lockheed Georgia Company
H.S. Sweet
Marietta, Georgia 30060

NASA Installations

NASA Headquarters
N.F. Rekos
Washington, D.C. 20546

NASA-Ames Research Center
L. Roberts
Moffett Field, California 94035

NASA-Flight Research Center
D.R. Scott
Edwards, California 93523

NASA-Langley Research Center
R. Kuhn
Hampton, Virginia 23665

NASA-Lewis Research Center
21000 Brookpark Road
Cleveland, Ohio 44135

E.F. Baehr
M.A. Beheim
D.N. Bowditch
L.J. Chelko
C.C. Ciepluch
E.W. Conrad
R.J. Denington
A. Ginsburg
M.J. Hartmann
R.H. Kemp
Lewis Library
R.W. Luidens
Report Control Office
L.W. Schopen
R.W. Schroeder
M.F. Valerino

NASA/Air Force Liaison
Wright Patterson Air Force Base
Dayton, Ohio 45433

L. Obery
C. Simpson
Col. C.E. Painter
G.K. Richey
G.P. Peterson

Pratt & Whitney Aircraft
Division of United Aircraft Corp.
J. Chew
20800 Center Ridge Road
Rocky River, Ohio 44116

Rohr Corporation
F. Hom
Box 878
Foot and H Street
Chula Vista, California 92012

Wyle Laboratories
L. Sutherland
128 Maryland Street
El Segundo, California 90245